Lab on a Chip

Accepted Manuscript

This is an *Accepted Manuscript*, which has been through the Royal Society of Chemistry peer review process and has been accepted for publication.

Accepted Manuscripts are published online shortly after acceptance, before technical editing, formatting and proof reading. Using this free service, authors can make their results available to the community, in citable form, before we publish the edited article. We will replace this *Accepted Manuscript* with the edited and formatted *Advance Article* as soon as it is available.

You can find more information about *Accepted Manuscripts* in the **Information for Authors**.

Investigation of different nanoparticles for

magnetophoretically enabled nanofin heat sinks in

microfluidics

Pyshar Yi, [*a] Khashayar Khoshmanesh,[*a] Jos L. Campbell,[b] Phillip Coughlan,[a]

Kamran Ghorbani,[a] and Kourosh Kalantar-zadeh[*a]

[a] RMIT University, School of Electrical and Computer Engineering, Melbourne, Victoria 3001, Australia.

[b] School of Applied Sciences, RMIT University, Melbourne, Victoria 3001, Australia.

E-mail: pyshar.yi@gmail.com,

kourosh.kalantar@rmit.edu.au,

khashayar.khoshmanesh@rmit.edu.au

19 **Abstract**

20 Assembled nanofin heat sinks, nanostructures which are formed *via* external forces in a cooling

21 microfluidic to remove heat from hot spots, is a new concept that has recently been introduced.

22 In this work we investigate nanofin structures formed by CrO_2 and Fe_2O_3 magnetic nanoparticles

23 and compare their performance. Thermal imaging are used for comparison of the three cases

24 including: (i) DI water as the coolant liquid, (ii) suspension of magnetic particles in DI water,

25 and (iii) suspension of magnetic particles in DI water in the presence of a magnetic field. For

26 each case, the experiments are conducted at three different flow rates of 10, 40 and 120 µl min^{-1}.

27 Our results suggest that the high thermal conductivity of the nanofins comprising of CrO_2

28 significantly enhances the heat exchange across the microchannel. The proof-of-concept

29 magnetophoretic system can offer a practical solution for the cooling of future compact

30 electronics.

31

32 **Keywords:** Cooling; heat exchange; hot spots; magnetophoresis; microfluidics; permanent

33 magnet

34

35

36

37

38

39

40

41

42 **Introduction**

43 Ever more packing of transistors into integrated circuits (ICs), in order to achieve higher

44 processing powers, signifies the problem of cooling of hot spots, which are generated during the

45 operation of these electronic systems. Without any proper thermal management, the temperatures

46 of these hot spots significantly rise, thus reducing the expected life and reliability of the ICs.

47 Hence, effective cooling of such compact systems has become a major challenge facing the

48 development of future electronic components[1, 2].

49 Cooling by means of liquid types such as water, ethylene glycol or various engine oils,

50 has been proposed to cool the hot spots in microchannels integrated with heat sinks[3, 4]. To date,

51 fin structure heat sinks with various geometries have been developed for cooling applications[5-7].

52 Further improvement in heat transfer has been achieved by growing high aspect ratio microfins

53 made of highly thermally conductivitive materials (including carbon nanotubes)[8, 9]. However,

54 this approach is costly, not quite compatible with many silicon industry standards, time

55 consuming and involves rather complicated fabrication processes.

56 To increase the thermal conductivity of the coolant fluid, nanoparticles are added to the

57 liquid forming suspensions known as "nanofluids"[10]. Implementing nanofluids are suggested to

58 be an attractive solution for cooling micro-scale devices[11-13]. Nevertheless, addition of

59 nanoparticles to the liquid has a limit, since high concentrations of nanoparticles increases the

60 viscosity of the fluid, causing a pressure drop and can even interrupt the flow passage by

61 clogging the microchannel[14-16]. To overcome such a problem, we can use other advantages that

62 exist from nanoparticle materials. Nanoparticles act as near free particles in liquid suspensions.

63 As a result, they can be manipulated to be aligned or trapped in specific locations of the

64 microchannel[17, 18]. By doing this, while the nanoparticles' concentration can be increased at the

65   desired location, whilst their average concentration within the microfluidic system can be kept at

66   a low magnitude to allow for facile liquid flow[19, 20].

67   Among nanofluids are ferrofluids that consist of nano-scale magnetic particles in a non-

68   magnetic liquid, and have been widely used for cooling of microelectronic devices[21-24]. In this

69   case, the suspended magnetic nanoparticles can be manipulated by external magnetic fields to

70   enhance heat transfer along the well aligned magnetic nanoparticles. Microelectromagnets can

71   produce high gradient magnetic fields in order to guide the target magnetic particles[25, 26].

72   We have previously shown that CrO_2 magnetic nanoparticles can be dynamically formed

73   onto the hot spots magnetophoretically to allow the efficient heat exchange with coolant liquid in

74   a microchannel[19]. We demonstrated the formation of bundles of micro-size and long fins from

75   the assembled nanoparticles, which we called nanofins, which could significantly enhance the

76   cooling process. This was due to the high aspect ratio of the fins and their flexible structure that

77   could allow the large interaction of the liquid coolant with them. This paper is an extension to

78   this previous work. We compare the performance of two different magnetophoretically

79   assembled nanoparticles: CrO_2 nanorods with high thermal conductivity as well as a long

80   morphological structure and Fe_2O_3 nanoparticles with a relatively lower thermal conductivity.

81   The thermal performance of the systems are assessed by measuring the temperature profiles

82   using an infrared camera. Extensive experimental and numerical analysis are conducted to

83   explore the effectiveness of these two model nanoparticles in forming nanofins at different flow

84   rates of the liquid.

85

86

87

88 **Experimental section**

89 **Magnetic particles preparation**

90 CrO_2 and Fe_2O_3 nanoparticles, were purchased from Sigma-Aldrich, Australia, and their typical

91 morphologies are shown in Fig. 1(a and b), respectively. CrO_2 nanoparticles have a rod- shape of

92 35 nm diameter and 250 nm length on average, while Fe_2O_3 nanoparticles are spherical with the

93 average diameter of 184 nm as confirmed by Distribution Light Scattering (DLS) system (ALV-

94 GmbH, Germany) (see Fig. S3). Separate solutions of CrO_2- Mili-Q water and Fe_2O_3-Mili-Q

95 water were prepared as detailed below.

96 Both dispersions were stablelized with trisodium citrate dehydrate ($Na_3C_6H_5O_7$, $2H_2O$) at

97 room temperature to avoid aggregation. To achieve this, trisodium citrate dehydrate 300 µl at

98 5 mg ml^{-1} was added to Mili-Q water 15 ml, and then the nanoparticles were added. This solution

99 was sonicated for 30 min to reduce aggregates. Next, the solution was placed in a thermo-mixer

100 at 70 °C with a speed of 600 rpm for 8 hours to functionalize the surface of each type of

101 nanoparticles with citric acid. The solution was then centrifuged at 8000 rpm for 15 min and

102 washed with Milli-Q water. This process was repeated three times, and the particles were re-

103 dispersed in 15 ml Milli-Q water to a concentration of suspended nanoparticles of 0.15% *w/w*.

104 We further diluted each solution 2.5 times in DI water, which reduced the final concentration to

105 0.06% *w/w* (0.012% *v/v*). Transmission Electron Microscopy (TEM, Jeol 1010 TEM) and

106 Scanning Electron Microscopy (FEI Nova SEM 650) were conducted to verify the size and shape

107 of the CrO_2 and Fe_2O_3 nanoparticles, respectively.

108

109

110

111

112 **Microfluidic device**

113 The magnetophoretic platform is schematically presented in Fig. 1(c). It consists of a

114 polydimethylsiloxane (PDMS) block, a heater and a glass slide. The microchannel dimensions

115 were set to 1500 μm × 280 μm × 40 mm (width×height×length). The channel height of 280 μm

116 was chosen to prevent any possible clogging of the microchannel after the entrapment of

117 nanoparticles. The microchannel was fabricated from PDMS using soft photolithography

118 techniques[27]. In doing so, SU8-3050 (Microchem, USA) layer was spin coated three times at

119 1000 rpm on a 3-inch diameter silicon wafer to produce a 280 µm thickness layer. The sample

120 was then exposed to UV light source using an MA6 mask aligner for 3 min with an interval of

121 1 min between each exposure, and developed in SU-8 developer for 40 min to realize the

122 patterns on the master. A 10 g mixture of PDMS base and curing agent (Sylgard 184, Dow

123 Corning) were mixed in a 10:1 weight ratio, and degassed in order to remove the trapped air

124 bubbles using a vacuum oven. The PDMS mixture was poured onto the master, such that it

125 covered the microchannel and cured on a hot plate with a temperature of 70 °C for 5 min.

126   Next, a small heater made by winding a Eurika wire (2.2 Ω/foot) around a 5 mm diameter

127 ceramic ring, was integrated onto the PDMS block. In order for heat to easily travel through the

128 microchannel, the heater was inserted 1 mm from a microchannel side wall. The rest of the

129 PDMS mixture was poured into the device to cover the heater. The device was cured for a further

130 15 min on the 70°C hot plate. The substrate was allowed to cool down for 5 min. The PDMS

131 block of 50 mm × 10 mm × 5 mm (length×width×height) was carefully peeled from the master.

132 The fabrication process was conducted in a class 1000 cleanroom.

133   The PDMS block was integrated onto a glass slide (Menzel-Glaser, USA) of 60 mm × 20

134 mm × 100 µm (length×width×height). The glass thickness of 100 µm was chosen to facilitate the

135 temperature measurement using infrared camera. Tygon® microtubes with an internal diameter

136   of 400 μm were placed into the holes punched within the PDMS block to interface with the

137   sample bottle and the syringe pump.

138

139   **Permanent magnet**

140   Three sheets of nikel plated neodymium magnet, which are used in standard hard disks of

141   computers, with dimension of 40 mm × 20 mm × 2 mm (length × width × height), were stacked

142   on top of each other to produce a total uniform magnetic field of ~0.36 T at the microchannel

143   region, as measured by a Teslameter (F. W. BELL, USA). The magnet stack was oriented in

144   such a way that its tip was exposed to the hot spot (Fig. 1(d)). The magnetic field drops with the

145   distance from the microchannel was measured and showed in Fig. S4.

146

147   **Apparatus**

148   Supplementary Fig. S1 shows an experimental setup of the microfluidic system. A syringe pump

149   (Harvard PHD 2000) was used for providing the flow through the microchannel. The syringe

150   pump was activated in refill mode to supply a suction force in order to prevent the leakage and

151   generation of bubbles within the microchannel. The heater was energized *via* a DC power supply

152   (Gw Instek, GPS-X303 series, Taiwan). Before each experiment, to prevent the adhesion of

153   CrO_2/Fe_2O_3 particles to the glass and PDMS surface, the channel was flushed with a 1% *w/w*

154   mixture of liquid surfactant (Triton X-305) for 10 min at a flow rate of 80 µl min^{-1} and then

155   washed with DI water for 10 min. The microfluidic device was mounted on an inverted

156   microscope (Nikon, Eclipse TE2000U, Japan) to observe the trapping of nanoparticles in time.

157   An infrared camera (Titanium Cedip Infrared Systems, France) was used for measuring the

158   temperature along the glass slide, which formed the bottom surface of the microchannel.
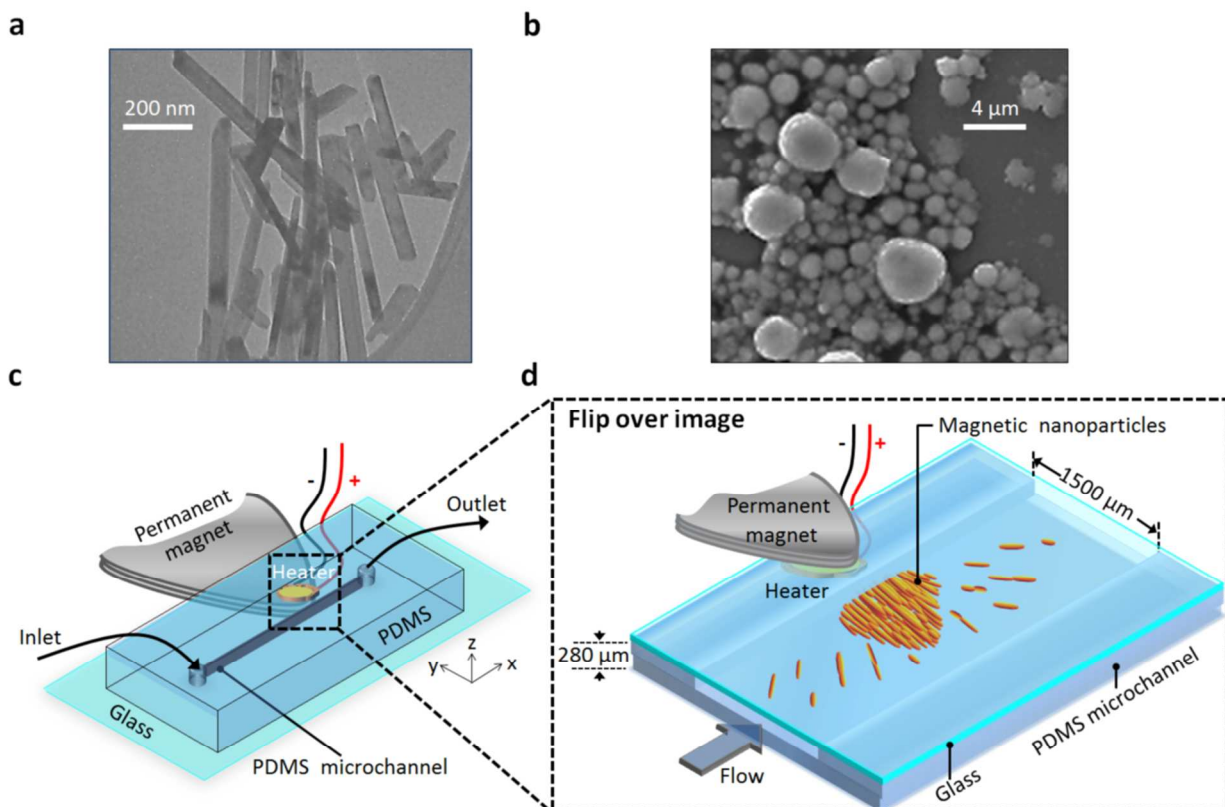
159

160 **Fig. 1** The microfluidic platform and magnetic nanoparticles. (a) TEM image of CrO_2

161 nanoparticles. (b) SEM image of Fe_2O_3 nanoparticles. (c) The schematics of microfluidic system

162 comprised of a PDMS block bonded to a 100 μm glass slide, an integrated heater, and a

163 permanent magnet. (d) The close up of the microchannel bottom view with trapped CrO_2

164 magnetic nanoparticles.

165

166

167

168

169

170

171

172   **Simulation details**

173   Extensive computational fluid dynamic (CFD) simulations were carried out to further analyse the

174   thermal performance of the magnetophoretic system. The simulations were conducted in both

175   three-dimensions and steady state using the ANSYS Fluent 6.3 (Canonsburg, PA, USA) software

176   package. This involved solving the differential equations governing the balance of mass,

177   momentum and energy to calculate the variations of velocity, pressure and temperature

178   throughout the microchannel, as given below:

$$\nabla \cdot \vec{U} = 0 \tag{1}$$

$$\rho_{suspension} \, (\vec{U} \cdot \nabla) \, \vec{U} = -\nabla P + \mu_{suspension} \, \nabla^2 \vec{U} \tag{2}$$

$$(\rho . c_p)_{suspension} \, (\vec{U} \cdot \nabla) \, T = k_{suspension} \nabla^2 T \tag{3}$$

179   where $\vec{U}$, P and T are the velocity, pressure and temperature of the suspension, ρ, μ, c_p and k are

180   the density, dynamic viscosity, heat capacity and thermal conductivity of the suspension. The

181   values of ρ, μ, c_p and k for the DI water, CrO_2 suspension, and Fe_2O_3 suspension are given, as

182   presented in the Supplementary Information 2.

183   The simulations involved solving the energy equation for the heater, PDMS block,

184   magnetically formed nanofins, and glass slide, as given below:

$$k_{heater} \, \nabla^2 T + \dot{Q}_{heater} = 0 \tag{4}$$

$$k_{PDMS} \, \nabla^2 T = 0 \tag{5}$$

$$k_{nanofin} \, \nabla^2 T = 0 \tag{6}$$

$$k_{glass} \, \nabla^2 T = 0 \tag{7}$$

185   where k_{heater}, k_{PDMS}, $k_{nanofin}$ and k_{glass} are the thermal conductivities of the heater, PDMS block,

186   nanofins and glass slide, respectively, while $\dot{Q}_{heater}$ is the source term representing the power

187   injected *via* the heater.

188   The boundary conditions used for calculating the variations of velocity and pressure

189   within the microchannel include the zero pressure at the inlet and the desired flow rate at the

190   outlet of the microchannel. No slip boundary condition was applied at the surfaces of the channel

191   for the pure liquid, which was replaced with the slip boundary condition for the CrO_2 or Fe_2O_3

192   suspensions, as detailed in our previous work[1]. The boundary conditions used for calculating the

193   variations of temperature within the solid parts included: the ambient temperature at the inlet of

194   the channel, a fully developed boundary condition at the outlet of the channel, and free

195   convection at the free surfaces of the system in contact with the surrounding environment with

196   the natural convection coefficient assumed to be 10 W m^{-2} K^{-1}. The value of $\dot{Q}_{heater}$ was

197   calculated by considering the injected power as 0.2 W.

198

199

200

201

202

203

204

205

206

207

208 **Results**

209 **Trapping characteristics of nanoparticles**

210 The trapping mechanism of CrO_2 and Fe_2O_3 nanoparticles was studied at the flow rates of 10, 40

211 and 120 µl min^{-1}. The permanent magnet was placed at the bottom of the device (Fig. 1(d)) to

212 provide a strong magnetic field within the microchannel. To minimize the heat conduction

213 between the hot glass slide and the surface of the permanent magnet, the magnet was isolated

214 from the glass by a 0.5 mm layer of rubber (Blu-Tack). Moreover, to ensure that the hot region

215 surrounding the heater is visible by the infrared camera, the tip of the magnet was placed 1.5 mm

216 from the microchannel (Fig. 2(a)). The heater was energized with a constant DC current of 0.5 A

217 and voltage of 0.4 V for 10 min to allow the system reach its steady state temperature before

218 applying the magnet.

219 Fig. 2(a) shows a schematic represents the microchannel. Fig. 2(b) demonstrates a flow of

220 DI water within the microchannel. Fig. 2(c-e) depict the CrO_2 nanoparticles trapped along the

221 side wall of the microchannel 10 min after the application of magnetic field (refer to

222 Supplementary Fig. S5 for Fe_2O_3 nanoparticles trapping under various flow rates). The images

223 were captured by a 4× microscope objective lens and assembled along the *x*-axis to demonstrate

224 the full picture.

225 Approaching the magnet, the nanoparticles began to form chains, were deflected towards

226 the side wall (near hot spot), and also docked perpendicular to the side wall (as demonstrated in

227 Fig. 2(f). The docked chains grew to form micro-sized bundles of CrO_2 nanoparticles (nanofins)

228 along the side wall with maximum lengths closer to the tip of the magnet (Fig. 2(f)).

229 At a low flow rate of 10 µl min^{-1}, the maximum width of nanofins reached 450 µm, or

230 30% of the microchannel width ($0.3W_{channel}$). At the same time, the total length of the nanofin

231 arrays reached ~4600 µm (i.e. ~3.1 $W_{channel}$). Interestingly, the maximum width and length of the

232 nanofins increased with an increase in flow rate Fig. 2(d and e). For example, at the flow rate of

233 40 µl min^{-1}, they increased to ~0.45 $W_{channel}$ and ~3.5 $W_{channel}$, respectively. Likewise, at a high

234 flow rate of 120 µl min^{-1}, they reached ~0.68 $W_{channel}$ and ~3.9 $W_{channel}$, respectively (see

235 Supplementary video-1 and 2 for the formation of CrO_2 and Fe_2O_3 nanofins at the above

236 conditions, respectively). The system had a saturation time, after which the growth of nanofins

237 was decelerated. Under the aforementioned conditions, the saturation was observed 8-10 min

238 after the application of the magnetic field. The nanofins can be washed away from the side wall

239 by removing the magnet and applying DI water to the microchannel at a flow rate of 200 µl min^{-1}

240 for 3 min. A full discussion on the dynamics of the nanofins can be found in our previous

241 work[19].

242
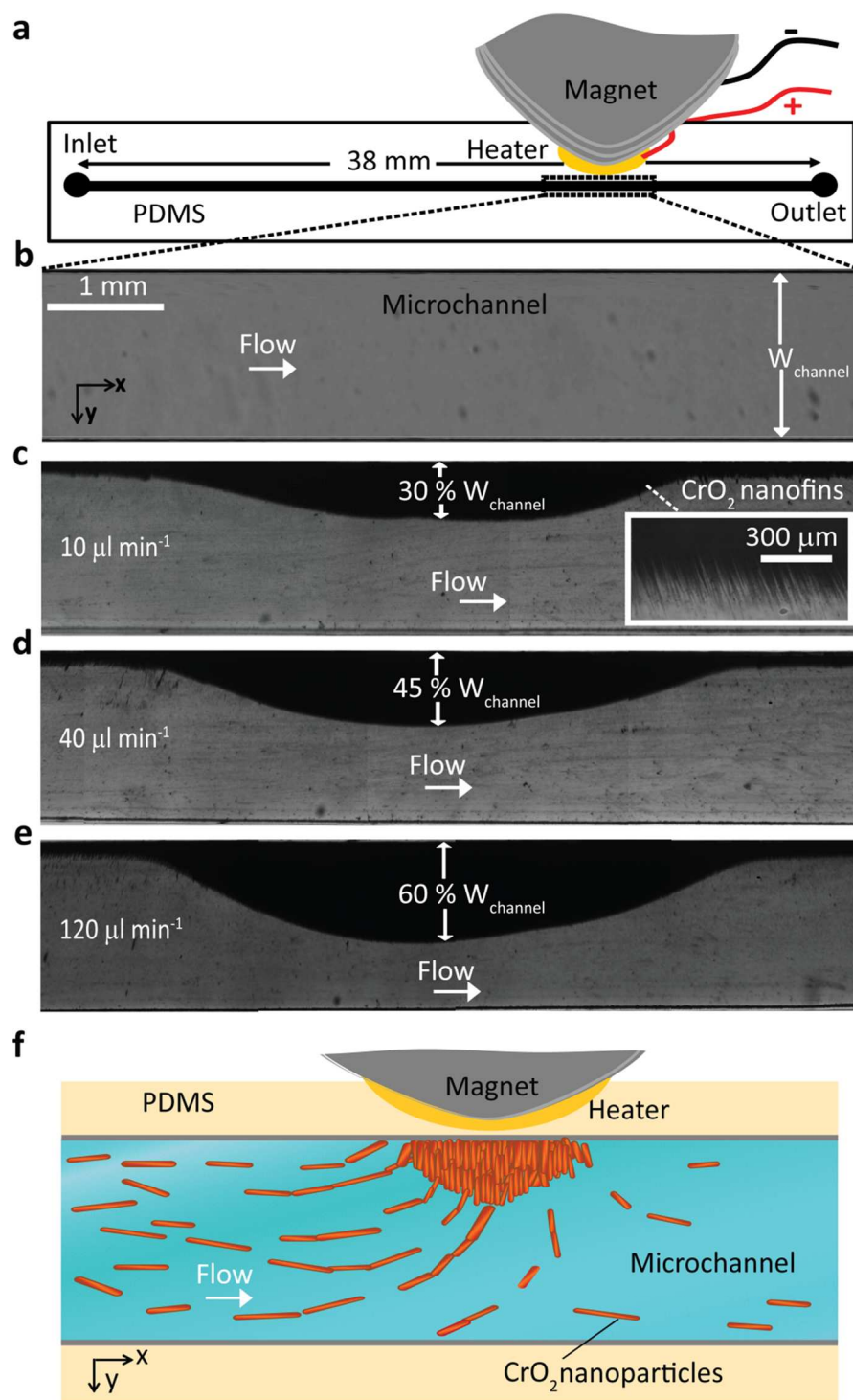
Fig. 2 (**a**) A schematic of the microchannel. Growing length of CrO_2 nanoparticles into nanofins

under the influence of the magnetic field at different flow rates of 10, 40, and 120 µl min^{-1} after

10 min. (**b**) A flow of DI water in the microchannel. (**c**) At 10 µl min^{-1} the length of CrO_2

246   nanofins were obtained to be 30% of the microchannel's width. The inset demonstrates a close

247   up image of the nanofins layer. (**d**) At 40 µl min^{-1} the length of CrO$_2$ nanofins were obtained to

248   be 45% of the microchannel's width. (**e**) At 120 µl min^{-1} the length of CrO$_2$ nanofins were

249   obtained to be 60% of the microchannel's width. (**f**) the schematic representing the growth of

250   nanofins.

251

252   **Thermal characterization of nanofins**

253   Next, we characterized the thermal performance of the magnetophoretic platform by obtaining

254   thermal images from the side of the 100 µm thick glass substrate using an infrared camera, as

255   described in our previous work[1]. The measurements were conducted at three different flow rates

256   of 10, 40 and 120 µl min^{-1}. The temperature of the fluid entering the microchannel followed the

257   ambient temperature, which was 298±0.3 K during the experiments. The heater was energized by

258   applying a DC signal of 0.5 A and 0.4 V. The results obtained at 40 and 120 µl min^{-1} are shown

259   here and the case involving a 10 µl min^{-1} flow rate is presented in the Supplementary Fig. S6.

260   The thermal imaging was conducted for the cases of (i) DI water, (ii) CrO$_2$ suspension

261   without permanent magnet, and (iii) CrO$_2$ suspension with permanent magnet (Fe$_2$O$_3$ suspension

262   thermal images are shown in Supplementary Fig. S7). For the case (iii), we used a permanent

263   magnet close to glass slide, as described in the previous section. However, for the cases (i) and

264   (ii) there was no magnetic field present. In order to mimic the same situations for these two cases

265   and capture comparable geometries by the infrared camera, we placed a 1 mm thick aluminum

266   plate exactly at the location of the permanent magnet (see Fig. 1(d)). The aluminum plate was

267   separated from the glass slide by a thin layer of rubber (Blu-Tack) to insulate it thermally. In

268   comparison to CrO$_2$, almost no change was discernible in thermal images of Fe$_2$O$_3$ suspensions

269   at similar cases. As a result, only the thermal profiles of Fe_2O_3 suspensions are shown in the next

270   section for comparison and discussion.

271   Fig. 3(a) shows a representation of the obtained temperature contours. Fig. 3(b-d) show

272   the obtained temperature contours at the glass surface for the aforementioned three cases at the

273   flow rate of   40 µl min^{-1}. The results were captured after 20 min, with 10 min to ensure the

274   system had reached a steady state temperature with the flow of DI water, and an extra 10 min to

275   ensure nanofin structures had been formed whilst subjected to the magnetic field with the

276   constant flow of nanoparticles. The heat, generated by the heater, was propagated through the

277   PDMS *via* conduction, as evidenced by the symmetric distribution of temperature contours

278   across the PDMS. However after reaching the microchannel, there was a competition between

279   the conduction and convection mechanisms to convey the heat.

280   In case (i), the hot side wall of the microchannel reached a maximum temperature of

281   313.8 K (Fig. 3(b)). At a high flow rate of 40 µl min^{-1}, the low thermal conductivity of DI water

282   led to a poor conduction through the microchannel, as evidenced by the stretching of temperature

283   contours towards the microchannel outlet (Fig. 3(b)). This led to a maximum temperature of

284   307 K at the opposite side of the microchannel and an average temperature of 304 K at the outlet

285   (Fig. 3(b)).

286   In case (ii), the heat exchange between the hot spot and the coolant fluid was improved

287   by adding CrO_2 nanoparticles (0.06% *w/w*) into the suspension. No magnetic field was applied in

288   this case. CrO_2 nanoparticles had a higher thermal conductivity than DI water, and increased the

289   overall thermal conductivity of the suspension, as evidenced by advancing the red contours

290   towards the opposite side wall and the outlet. This increased the maximum temperatures of the

291   hot and cold side wall to 315 K, and 308 K, respectively, while the average outlet temperature

292   increased to 304.6 K microchannel (Fig. 3(c)). Similar effects have been demonstrated by other

293   researchers[28-31].

294   In case (iii), a permanent magnet was applied to the system. The magnet generated a

295   magnetic field and caused CrO_2 nanoparticle to form chains which eventually created nanofins at

296   the hot spot, as shown in Fig. 2(c). Given the high thermal conductivity of nanofins

297    $(31 \text{ W m}^{-1} \text{ K}^{-1})$ [32], they provided an efficient path to conduct the heat from the hot side wall

298   towards the core of the microchannel, as evidenced by further advancing of red contours towards

299   the opposite side wall and the outlet (Fig. 3(d)). This increased the maximum temperature along

300   the hot and cold side walls to 316 K and 308 K, respectively while the average outlet temperature

301   increased to 306.5 K.

302   Fig. 3(e-g) show the obtained temperature contours at the glass surface for the three cases

303   at the flow rate of 120 µl min^{-1}. Likewise, these results were captured 10 min after the system

304   had reached its steady state temperature. Similar trends were observed in the temperature

305   contours before and after the addition of nanoparticles and also after applying the magnetic field.

306   However, increasing the flow rate to 120 µl min^{-1} enhanced the convective heat transfer across

307   the microchannel, which resulted in a general temperature drop across the microfluidic platform

308   (Fig. 3(e-g)).

309   Simulations are also conducted to verify and further discuss the performance of the

310   systems with and without nanoparticles as well as in conditions in which the CrO_2 nanoparticles

311   are trapped in the presence of a magnetic field, and form nanofins. The optimum flow rate of

312   120 µl min^{-1} is used for these simulations. Additionally, in order to compare the results, and

313   assess the conditions for increasing the thermal exchanges between the hot spot and the liquid

314   coolant in the channel, a set of thermal performance analyses was conducted by investigating the

315   temperature profiles along the parallel lines to the side walls, which are presented in the next

316   section.
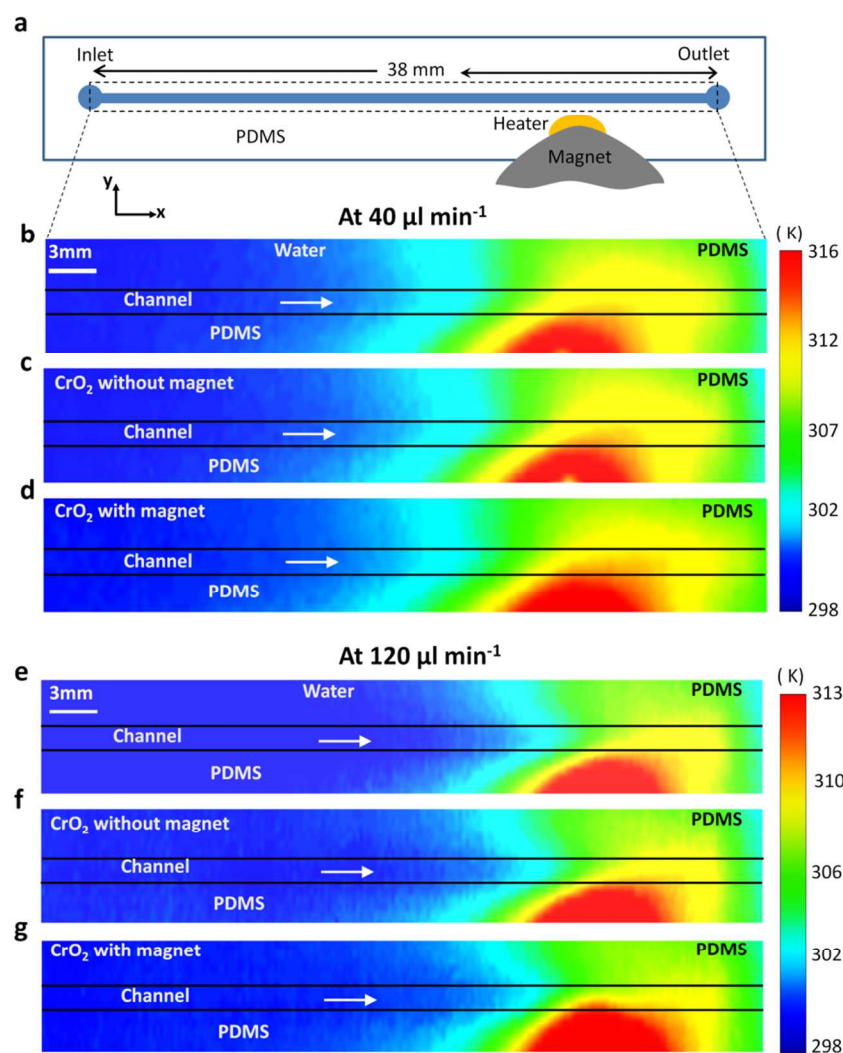
317

318   **Fig. 3 (a**) Schematics of the microchannel. Contours of temperature along the glass slide,

319   obtained by infrared camera at flow rates of 40 and 120 µl min^{-1} for the cases of: (**b**) Water

320   flowing through the microchannel. (**c**) CrO$_2$ nanoparticle suspension in the absence of the

321   magnet. (**d**) CrO$_2$ nanoparticle suspension in the presence of the magnet, forming CrO$_2$ nanofins

322   along the side wall. (**e**) Water flowing through the microchannel. (**f)** CrO$_2$ nanoparticle

323   suspension in the absence of the magnet. (**g**) CrO_2 nanoparticle suspension in the presence of the

324   magnet, forming nanofins.

325

326   **Numerical simulation results**

327   Simulations were conducted at a flow rate of 120 µl min^{-1} and in three different cases to be in

328   line with the experiments: (i) DI water flowing through the channel, (ii) a suspension of CrO_2

329   nanoparticles flowing through the channel, and (iii) a suspension of CrO_2 nanoparticles flowing

330   through the channel while a CrO_2 nanofin structure is formed along the hot side wall.

331   Fig. 4 shows the simulated temperature contours along the external surface of the glass

332   slide (which was experimentally measured using the thermal imaging camera) as well as along

333   the plane normal to the microchannel, which passes through the heater and magnetically formed

334   nanofins (which cannot be measured using the thermal imaging camera).

335   For case (i), the simulations indicated the propagation of heat towards the microchannel,

336   which was associated with the deflection of temperature contours towards the right (Fig. 4(a)),

337   which was also confirmed in the thermal imaging experiments. The cross sectional contours

338   indicated that the temperature does not significantly change along the thickness of the glass slide

339   and the height of channel. This means that the temperature contours obtained by thermal imaging

340   camera could correctly obtain the temperature variations across the channel (Fig. 4(b)).

341   However, a sharp temperature drop of 6.1 K was obtained across the width of the channel,

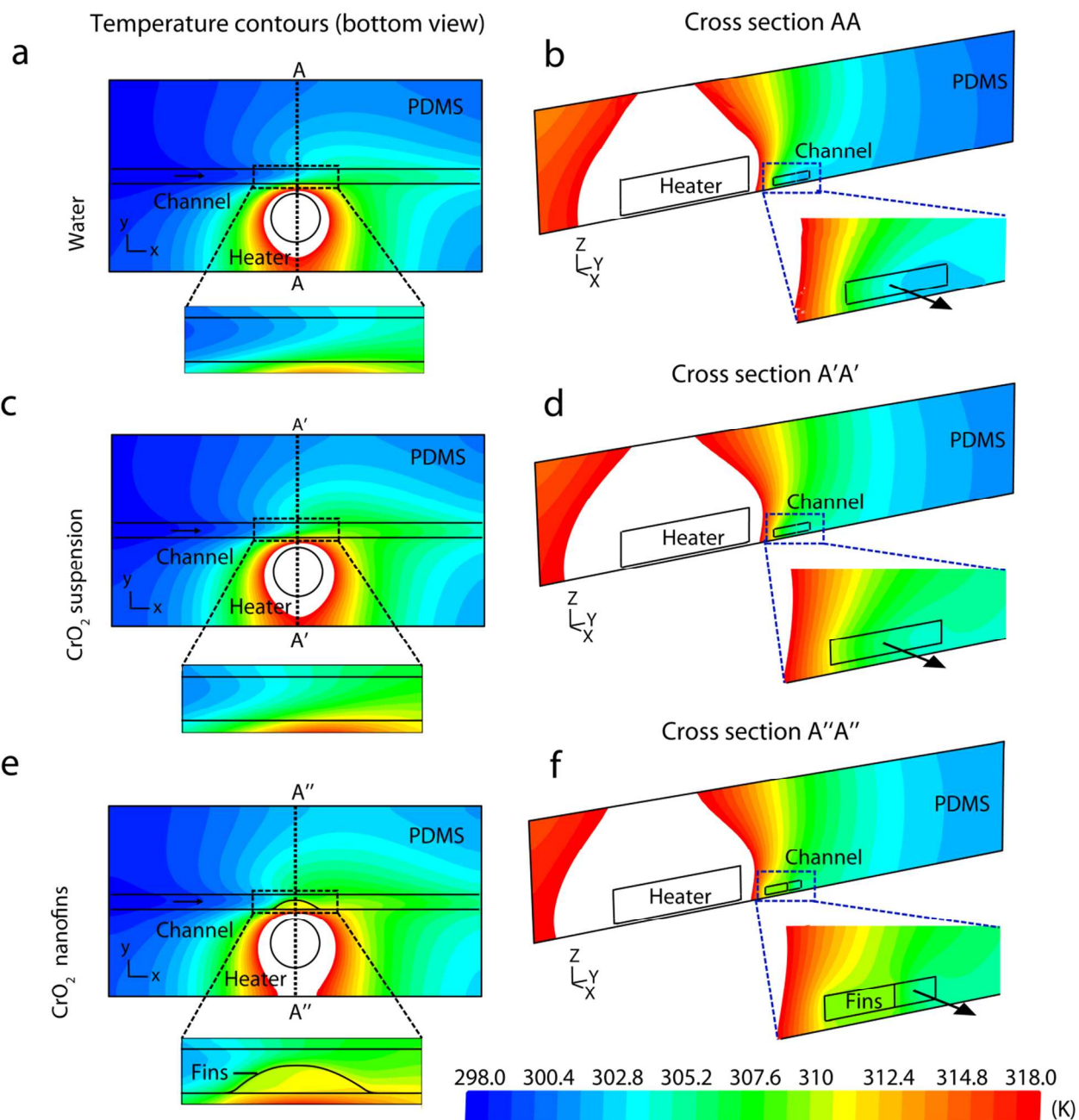342   indicating the dominance of convection (Fig. 4(b)).

343   For case (ii), the heat was more smoothly propagated within the system, as evidenced by

344   advancement of 'yellow' and 'green' bands towards the microchannel, and also the receding of

345   the 'blue' band along the channel (Fig. 4(c)). Moreover, the temperature drop across the width of

346   the channel reduced to 5.05 K, indicating the improvement of the thermal conduction through the

347   channel (Fig. 4(d)).

348   For case (iii), the nanofin bundles were simulated using a structure (the conditions of this

349   structure are presented in our previous work[19] formed adjacent to the hot side wall of the

350   microchannel with a geometry similar to that obtained in experiment (Fig. 2(e)), which extended

351   along the height of the channel. The simulations revealed that the formation of the CrO_2 nanofins

352   led to better propagation of heat through the entire microfluidic system, as evidenced by the

353   formation of a 'yellow' region at the location of nanofins, as also the receding of the 'blue' band

354   along the channel (Fig. 4(e)). More interestingly, the temperature drop across the width of the

355   channel reduced to 3.15 K (Fig. 4(f)). In other words, the incorporation of CrO_2 nanofins resulted

356   in an increase of a forced convection through the microchannel and also the free convection

357   across the free surfaces of PDMS block and the glass slide, which in turn avoided the

358   accumulation of heat at the hot spot.

359

360

Temperature contours (bottom view)

a Water

b Cross section AA

c CrO$_2$ suspension

d Cross section A'A'

e CrO$_2$ nanofins

f Cross section A''A''

298.0 300.4 302.8 305.2 307.6 310 312.4 314.8 318.0 (K)

361

Fig. 4 Simulation results for heat transfer within the magnetophoretic system. The flow rate of

the outlet is set to 120 µl min^{-1} while the temperature of the liquid at the inlet is set to 298 K.

Temperature contours across the glass slide and cross section of the microchannel for the case of:

(**a-b**) water. (**c-d**) CrO$_2$ nanoparticles suspension in the absence of magnet and (**e-f**) magnetically

assembled CrO$_2$ nanofins.

Thermal performance of CrO_2 vs. Fe_2O_3 nanofins

367

368   To further explore the effectiveness of CrO_2 and Fe_2O_3 nanofin structures, we studied the

369   thermal performance of the system under different flow rates of 10, 40 and 120 µl min^{-1}. In all

370   cases, the heater was energized by applying a DC signal of 0.5 A and 0.4 V. Both nanoparticle

371   suspensions were applied under the same concentration (0.06% *w/w*), and the results were

372   obtained after 10 min. The variations of temperature were examined along nine parallel lines

373   across the channel including both side walls, thus there was a gap of 187.5 µm gap between the

374   lines. At each flow rate, temperature variations were studied for the cases of (i) DI water, (ii)

375   CrO_2 nanoparticle suspension without magnet, (iii) CrO_2 nanoparticle suspension with magnet,

376   (iv) Fe_2O_3 nanoparticle suspension without magnet, and (v) Fe_2O_3 nanoparticle suspension with

377   magnet. When comparing different cases, we focused on three characteristic temperatures of the

378   system, including: the maximum temperature of the channel side wall close to the heater, T_{hot},

379   the maximum temperature of the channel side wall far from the heater, T_{cold}, and the average

380   temperature of the outlet, T_{outlet}. Here, we demonstrate the thermal performance of the system at

381   the flow rates of 40 and 120 µl min^{-1}, while the results obtained at a low flow rate of 10 µl min^{-1}

382   are given in Supplementary Fig. S9. For the case involving the constant flow rate of 10 µl min^{-1},

383   the conduction was more dominant than the convection so it could not be directly compared to

384   40 and 120 µl min^{-1} cases.

385   　　　At a low flow rate of 40 µl min^{-1}, application of DI water case (i), led to the following

386   temperatures along the microchannel: $T_{hot} = 313.5$ K, $T_{cold} = 307$ K and $T_{outlet} = 304$ K (Fig. 5(a)).

387   Alternatively, addition of CrO_2 nanoparticles to DI water case (ii), led to a slight increase of

388   temperatures along the microchannel: $T_{hot} = 315$ K, $T_{cold} = 308$ K and $T_{outlet} = 304.6$ K (Fig. 5(b)),

389   which can be attributed to higher thermal conductivity of the suspension. Interestingly, the

390   activation of the magnetic field in the presence of CrO_2 nanoparticle suspension case (iii), led to

391   further increase of temperatures along the microchannel: $T_{hot} = 316$ K, $T_{cold} = 308$ K and $T_{outlet} =$

392   306.5 K (Fig. 5(c)), which can be attributed to strong conduction along the patterned nanofin

393   structure. The extent of the formed nanofin is shown in the graph. Moreover, a temperature drop

394   of 4 K was observed from the base to the tip of the nanofin.

395   Increasing the flow rate to 120 µl min^{-1}, enhanced the convective heat transfer through

396   the microchannel, and thus reduced the overall temperature across the system. For the case of DI

397   water, case (i), the following temperatures were measured along the microchannel: $T_{hot} = 309$ K,

398    $T_{cold} = 304$ K and $T_{outlet} = 303.3$ K (Fig. 5(a)). Addition of CrO_2 nanoparticles to DI water,

399   case (ii), slightly increased the temperatures along the microchannel: $T_{hot} = 310$ K, $T_{cold} = 304$ K

400   and $T_{outlet} = 304$ K (Fig. 5(b)), as observed before. Activation of magnetic field in the presence of

401   CrO_2 nanoparticle suspension, case (iii), further increased the temperature along the

402   microchannel: $T_{hot} = 313$ K, $T_{cold} = 304$ K and $T_{outlet} = 304.2$ K (Fig. 5(c)). Moreover, the

403   temperature drop from the base to the tip of the nanofin increased to 6.4 K.

404   In contrast, the addition of Fe_2O_3 nanoparticles to DI water, case (iv), led to almost

405   similar trends observed for the DI water at both flow rates of 40 and 120 µl min^{-1} (Fig. 5(d)).

406   However, activation of magnetic field in the presence of Fe_2O_3 nanoparticle suspension, case (v),

407   increased the overall temperature along the microchannel: $T_{hot} = 314$ K, $T_{cold} = 306.2$ K and

408    $T_{outlet} = 304.2$ K at a flow rate of 40 µl min^{-1} (Fig. 5(e)). Moreover, a temperature drop of 4.5 K

409   was observed from the base to the tip of the Fe_2O_3 nanofin. Compared to the case of CrO_2

410   nanoparticle suspension, case (iii), temperature increase was less, which can be attributed to the

411   low thermal conductivity of Fe_2O_3 nanoparticles (6 W m^{-1} K^{-1}) [33] compared to CrO_2 nanoparticles

412   (31 W m^{-1} K^{-1}) [32]. Moreover, the spherical structure of Fe_2O_3 nanoparticles led to more phonon

413   scattering, which in turn could cause a heat loss along the chains. In contrast, the CrO_2

414   nanoparticles had a rod-shape structure, as shown in SEM images (Fig. 1(a)), allowing phonons

415   to propagate with minimal scattering, which imposed less heat loss along the chains. Increasing

416   the flow rate to 120 µl min^{-1} led to similar trends and the following temperatures were measured

417   along the microchannel: T_{hot} = 311 K, T_{cold} = 304.2 K and T_{outlet} = 303.5 K at a flow rate of

418   40 µl min^{-1} (Fig. 5(e)). The temperature drop from the base to the tip of the Fe_2O_3 nanofin

419   increased to 7 K.

420   A set of experiments were conducted to observe the formation of the nanofin bundles at

421   different widths of the microfluidic channel, which is presented in Supplementary Information 9.

422   A study on the effect of various morphologies (aspect ratios) of CrO_2 and Fe_2O_3 on thermal

423   conductivity of nanofins is shown in Supplementary Information 3. The results indicate that an

424   elongated morphology such as rod-shaped (CrO_2) performs better for heat conduction

425   (Supplementary Fig. S2).

426

427

428

429
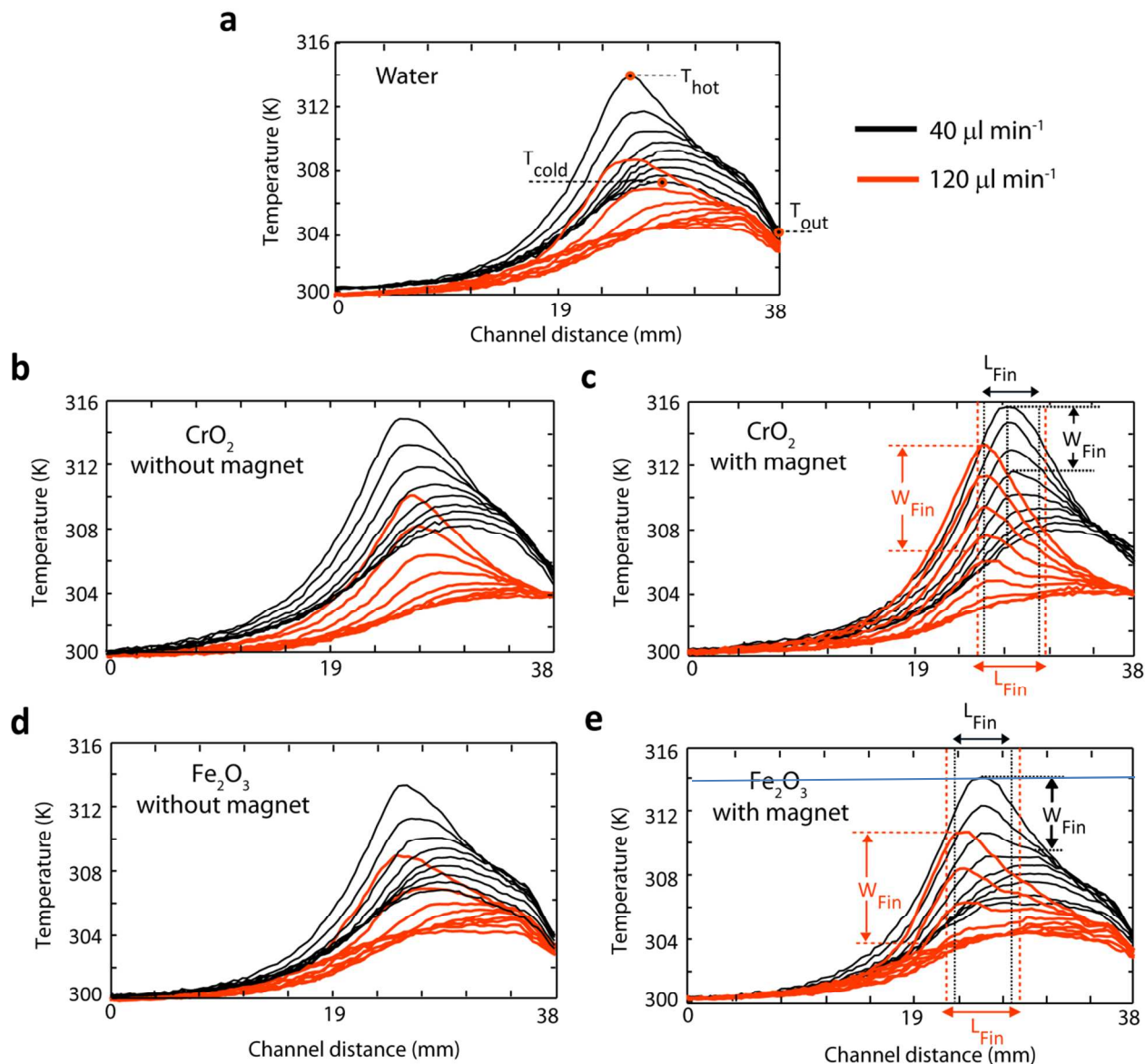
Fig. 5 Thermal effect of Fe_2O_3 and CrO_2 nanofins along the microchannel at flow rates of 40 and

120 µl min^{-1}: (**a**) DI water, (**b**) CrO_2 nanoparticles suspension without applying the magnet, (**c**)

CrO_2 nanofins after applying the magnet, (**d**) Fe_2O_3 nanoparticles suspension without applying

the magnet, and (**e**) Fe_2O_3 nanofins after applying the magnet.

434

435

436   In the last stage of the experiments, the study of different size Fe_2O_3 nanoparticles in

437   liquid was conducted to observe the effect of the size of the particles forming the nanofin

438   bundles on the heat transfer. The particles were separated using filters of different sizes. As a

439   result, three different suspension solutions were obtained for comparison. DLS was used for

440   measuring the average diameter of the particles suspended in DI water for three different samples

441   (see Supplementary Information 4): (1) no filter with the average diameter of 184 nm, (2) filter

442   with the porosity of 450 nm that resulted in the average diameter 128 nm and (3) 220 nm porous

443   to obtain particles of average diameter of 106 nm.

444   The experiments were carried out at the flow rate of 40 µl min^{-1}. The results are shown in

445   Figs. 6 and 7. As can be seen in Fig. 6, after 10 min the nanofins height reached 50%, 56% and

446   67% of the channel width for suspensions of 184 nm, 128 nm and 106 nm particles, respectively.

447   As can be seen in Fig. 7, the nanofins formed using the smaller particles (106 nm) shows an

448   improvement in heat transfer and the maximum temperature (T_{cold}) at the opposite side wall of

449   the microchannel was increased by ~2 K compared to the nanofins formed by the larger

450   nanoparticles (184 nm). This better heat transfer for smaller particles can be attributed to two

451   reasons. Longer nanofins are formed that can more efficiently transfer the heat into and other

452   side of the microchannel as well as the fact that more nanoparticles are in intimate contact with

453   each other, which promoted the thermal conductivity.

454
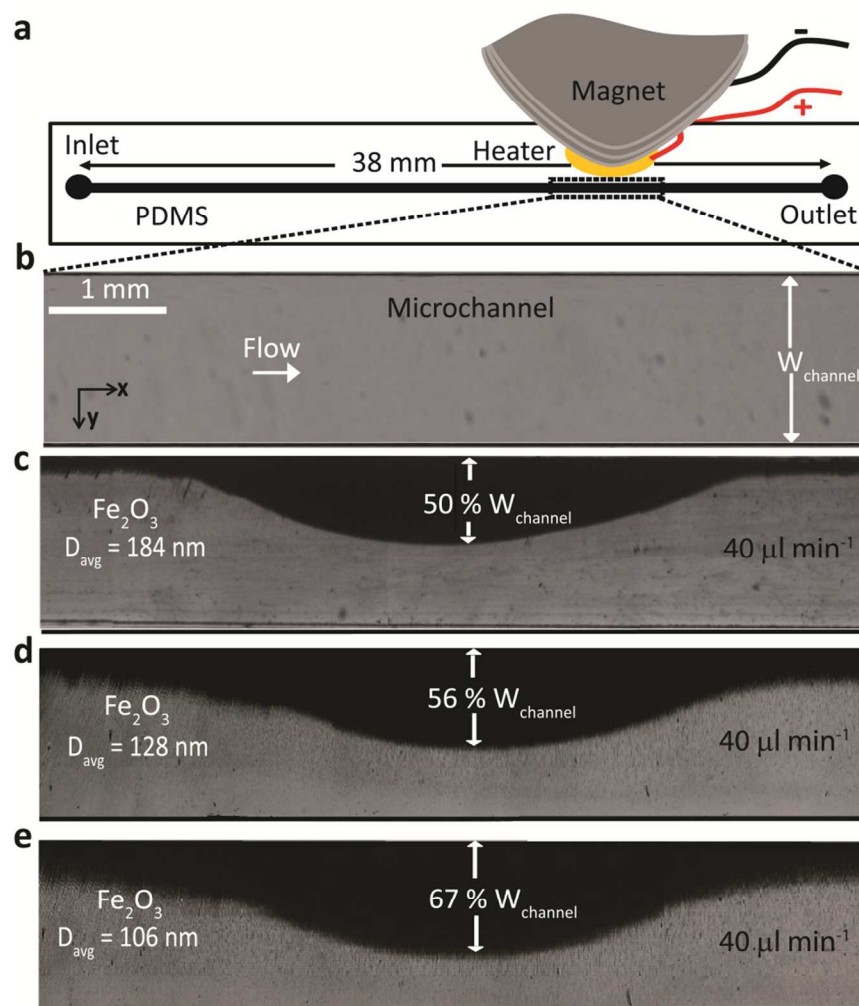
Fig. 6 (**a**) A schematic of the microchannel. (**b**) A flow of DI water representing the trapped

section of nanoparticles. Growing length of Fe_2O_3 nanoparticle bundles (nanofins) under the

influence of the magnetic field at a flow rate of 40 µl min^{-1} after 10 min for the cases of: (**c**) With

184 nm average sized Fe_2O_3 nanoparticles, the length of Fe_2O_3 fins was obtained to be 50% of

the microchannel's width. (**d**) With 128 nm average sized Fe_2O_3 nanoparticles, the length of

Fe_2O_3 fins was obtained to be 56% of the microchannel's width. (**e**) With 106 nm average sized

Fe_2O_3 nanoparticles, the length of Fe_2O_3 fins reached 67% of the microchannel's width.

462

463
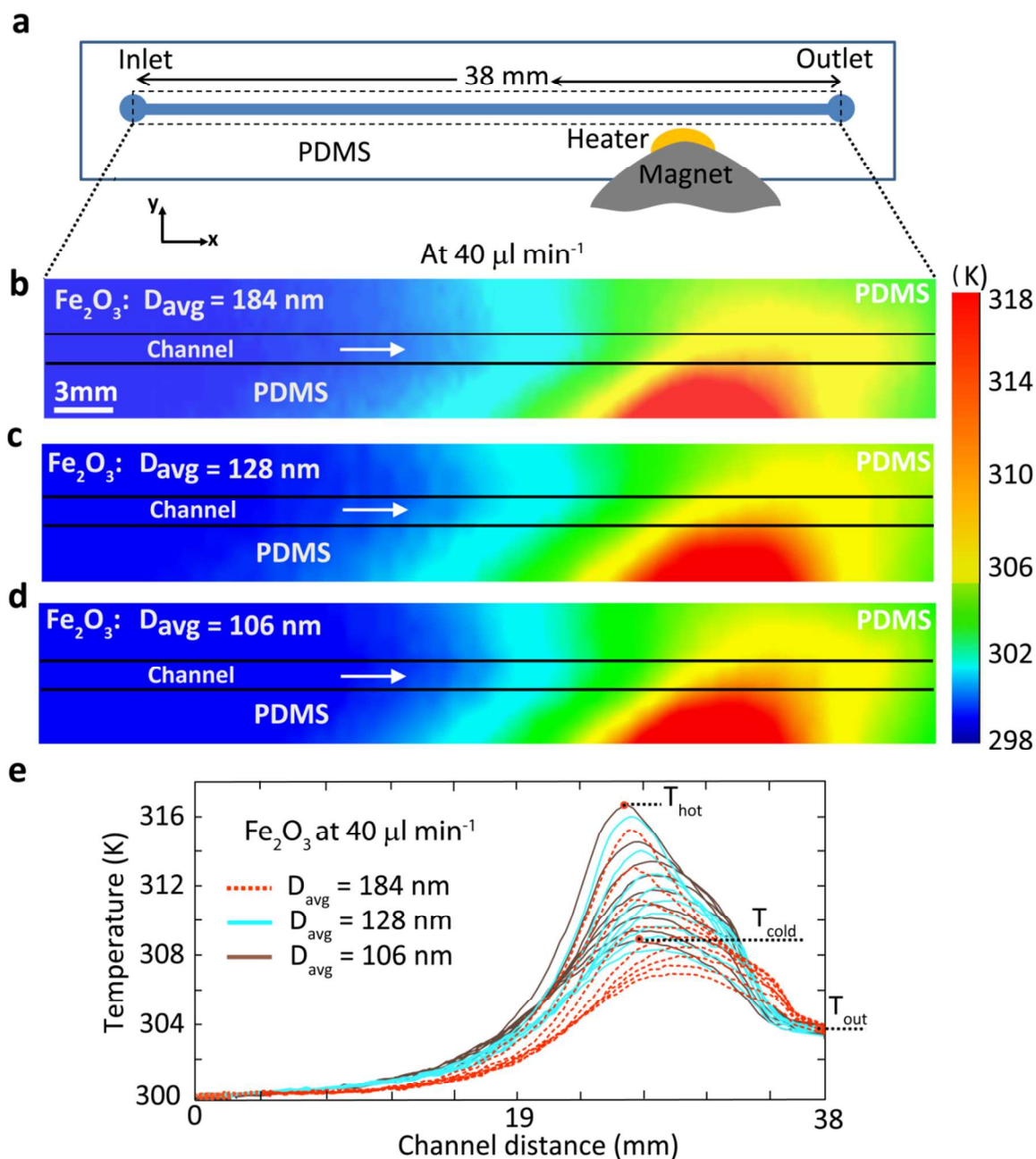
Fig. 7 (**a**) Schematics of microchannel. Temperature contours along the glass slide obtained

using infrared camera at flow rates of 40 µl min^{-1} for the cases with average diameters of: (**b**)

184 nm, (**c**) 128 nm, and (**d**) 106 nm Fe$_2$O$_3$ nanoparticles, respectively. (e) Temperature

distribution for different size of Fe$_2$O$_3$ nanoparticles forming nanofins along the microchannel at

flow rates of 40 µl min^{-1}(the temperature profiles are taken similar to those of Fig. 5)

469   **Conclusion**

470   This work presents a magnetophoretic system to enhance the heat exchange in a microfluidic

471   platform with an embedded heater. Experiments with CrO_2 and Fe_2O_3 nanoparticles indicate that

472   magnetically formed nanofins can be established along the walls of the microchannel upon the

473   application of a magnetic field. The nanofins are quite stable and their configurations do not

474   significantly change by increasing the flow rate from 10 to 120 µl min^{-1}. CrO_2 nanoparticles have

475   a higher thermal conductivity and are rod-shaped, and therefore the nanofins made of CrO_2

476   perform better than their Fe_2O_3 counterparts, which are comprehensively discussed in the paper.

477   The spherical Fe_2O_3 nanoparticles' cooling effect was minimal due to their low thermal

478   conductivity and high phonon scattering, which in turn reduce their efficiency. Compared to the

479   case of DI water as the coolant fluid, the formation of CrO_2 nanofins can increase the maximum

480   temperature of the hot side wall and the average temperature of the outlet by 2.5 and 2.5 K,

481   respectively, at a flow rate of 40 µl min^{-1}, and by 4 and 0.9 K, respectively, at a flow rate of

482   120 µl min^{-1}. This means that the heat conduction across the nanofins leads to better propagation

483   of heat across the platform, reducing the temperature at hot spots. The outcomes of this paper

484   show the importance of the selection type and morphology of nanoparticles in forming nanofins

485   for cooling applications.

486

487

488

489

490

491

499   **References**

500   1   P. Yi, A. A. Kayani, A. F. Chrimes, K. Ghorbani, S. Nahavandi, K. Kalantar-zadeh and
501   K. Khoshmanesh, *Lab on a Chip*, 2012, **12**, 2520-2525.
502   2   P. Ball, *Nature*, 2012, **492**, 174-176.
503   3   A. Bar-Cohen, M. Arik and M. Ohadi, *Proceedings of the IEEE*, 2006, **94**, 1549-1570.
504   4   H. B. Jang, I. Yoon, C. H. Kim, S. Shin and S. W. Chung, *IEEE International
505   Conference*, **2009,** 472-478.
506   5   S. J. Kim, *Heat Transfer Engineering*, 2004, **25**, 37-49.
507   6   Y. Peles, A. Kosar, C. Mishra, C. J. Kuo and B. Schneider, *International Journal of Heat
508   and Mass Transfer*, 2005, **48**, 3615-3627.
509   7   C. Y. Zhao and T. J. Lu, *International Journal of Heat and Mass Transfer*, 2002, **45**,
510   4857-4869.
511   8   F. Yifeng, W. Teng, L. Johan, W. Xiaojing and Z. Yan, *IEEE-Nano*, 2009, 44-49.
512   9   K. Kordas, G. Toth, P. Moilanen, M. Kumpumaki, J. Vahakangas, A. Uusimaki, R. Vajtai
513   and P. M. Ajayan, *Applied Physics Letters*, 2007, **90**, 123105.
514   10   D. B. Tuckerman and R. F. W. Pease, *Electron Device Letters*, 1981, **2**, 126-129.
515   11   O. Manca, Y. Jaluria and a. D. Poulikakos, *Advanes in Mechanical Engineering*, 2010,
516   **2010**, 1-2.
517   12   C. Kleinstreuer and Y. Feng, *Nanoscale Research Letters*, 2011, **6,** 229.
518   13   A. Ijam and R. Saidur, *Applied Thermal Engineering*, 2012, **32**, 76-82.
519   14   M. Chandrasekar, S. Suresh and A. C. Bose, *Experimental Thermal and Fluid Science*,
520   2010, **34**, 210-216.
521   15   S. Ozerinc, S. Kakac and A. G. Yazicioglu, *Microfluidics and Nanofluidics*, 2009, **8**, 145-
522   170.
523   16   X. Wu, H. Wu and a. P. Cheng, *Journal of Micromechanics Micorengineering*, 2009, **19,**
524   105020.
525   17   M. Horton, H. Hong, C. Li, B. Shi, G. P. Peterson and S. Jin, *Journal of Applied Physics*,
526   2010, **107**, 104320.
527   18   C. L. Altan, A. Elkatmis, M. Yuksel, N. Aslan and S. Bucak, *Journal of Applied Physics*,
528   2011, **110,** 093917.

529 19   P. Yi, K. Khoshmanesh, A. F. Chrimes, J. L. Campbell, K. Ghorbani, S. Nahavandi, G.
530   Rosengarten and K. Kalantar-zadeh, *Advanced Energy Materials*, 2014, Article in press,
531   DOI: 10.1002/aenm.201300537.
532 20   A. A. Kayani, K. Khoshmanesh, S. A. Ward, A. Mitchell and K. Kalantar-zadeh,
533   *Biomicrofluidics*, 2012, **6**, 031501
534 21   N. Pamme, *Lab on a Chip*, 2006, **6**, 24-38.
535 22   A. Gavili, F. Zabihi, T. D. Isfahani and J. Sabbaghzadeh, *Experimental Thermal and*
536   *Fluid Science*, 2012, **41**, 94-98.
537 23   Elwood D. Carlson, *Encyclopedia of Nanotechnology*, 2009, **1**, **Technology and**
538   **Engieering**, 1597.
539 24   B. Wright, D. Thomas, H. Hong, L. Groven, J. Puszynski, E. Duke, X. Ye and S. Jin,
540   *Applied Physics Letters*, 2007, **91,** 885-893.
541 25   K. Smistrup, O. Hansen, H. Bruus and M. F. Hansen, *Journal of Magnetism and*
542   *Magnetic Materials*, 2005, **293**, 597-604.
543 26   T. P. Forbes and S. P. Forry, *Lab on a Chip*, 2012, **12**, 1471-1479.
544 27   K. Khoshmanesh, C. Zhang, F. J. Tovar-Lopez, S. Nahavandi, S. Baratchi, K. Kalantar-
545   zadeh and A. Mitchell, *Electrophoresis*, 2009, **30**, 3707-3717.
546 28   J.-Y. Jung, H.-S. Oh and H.-Y. Kwak, *International Journal of Heat and Mass Transfer*,
547   2009, **52**, 466-472.
548 29   M. Ghazvini and H. Shokouhmand, *Energy Conversion and Management*, 2009, **50**,
549   2373-2380.
550 30   W. Duangthongsuk, A. S. Dalkilic and S. Wongwises, *Current Nanoscience*, 2012, **8**,
551   317-322.
552 31   Y. Fan, X. L. Zhong, J. Liu, T. Wang, Y. Zhang and Z. N. Cheng, *Microsystem*
553   *Technologies-Micro-and Nanosystems-Information Storage and Processing Systems*,
554   2009, **15**, 375-381.
555 32   P. Nordblad, *Nature Mater*, 2013, **12**, 11-12.
556 33   J. F. Shackelford and W. Alexander, *CRC Materials Science and Engineering Handbook*,
557   **2001**.

558

559

This work presents the thermal performance of a microfluidic system in the presence of magnetically formed nanofins (CrO_2 and Fe_2O_3).